Materials Advances

ROYAL SOCIETY OF CHEMISTRY

PAPER

View Article Online
View Journal | View Issue

Cite this: *Mater. Adv.*, 2024, 5, 3411

Designing multifunctional organic thermochromic ferroelectric materials: remarkable melt-cool large thermal hysteresis of reversible single crystal to single crystal transformation†

Rekha Kumari,[ac] Arnab De,[b] Aninda Jiban Bhattacharyya [ac] and T. N. Guru Row *[a]

Oxazolidinone-based organic ferroelectric compounds, namely (*E*)-4-(4-(benzylideneamino)benzyl)oxazolidin-2-one (BOA) and (*E*)-4-(4-(2-hydroxybenzylideneamino)benzyl)oxazolidin-2-one (HBOA), were synthesized. Both molecules have shown a reversible melting and solidification transformation from −50 °C to 250 °C as confirmed by differential scanning calorimetry (DSC) analysis. A large thermal hysteresis window of 100 °C and 87 °C was observed for BOA and HBOA, respectively, along with thermo chromic features. Variable temperature single crystal X-ray diffraction analysis reveals that an order–disorder transformation occurs for BOA while HBOA remains unchanged. Interestingly, both compounds exhibit significant reversible mechano-fluorochromic (MFC) behavior upon grinding and fuming. The reversible MFC behavior was confirmed by cognate techniques like powder X-ray diffraction (PXRD), thermal analysis and fluorescence studies. Furthermore, the systems were investigated to demonstrate the structure–property relationship in realizing their ferroelectric behavior by SHG, PUND (positive up and negative down) and RT (room temperature) and HT (high temperature) thermal responses of PE and dielectric measurements. BOA and HBOA show ferroelectric hysteresis loops at high electric fields with a high voltage tolerance (up to 181 kV cm^{-1}). By measuring the PFM hysteresis loops at various V_{dc} frequencies, an explicit V_c could be found in the ferroelectric rather than in the non-ferroelectric material. These findings provide a potential perspective for designing new organic multifunctional materials for applications in light displaying and memory devices.

Received 30th November 2023,
Accepted 25th February 2024

DOI: 10.1039/d3ma01073b

rsc.li/materials-advances

Introduction

The design and development of ferroelectric materials that exhibit reversible melting and solidification behaviour with large thermal hysteresis have drawn incredible attention in recent years due to their important applications in temperature controlling materials, ferro-elastic materials, switchable dielectric materials and memory devices.[1] In spite of their potential, very few organic compounds are known to exhibit a ferroelectric transition. From last few decades, several studies have focused on the thermally switchable electrical behaviour in organic ferroelectric materials.[2–10] Molecular materials that demonstrate switchable physical properties in response to external stimuli are fascinating for their potential applications in sensors, switches and memory media.[11–15] It is observed that in organic ferroelectric materials, the polarization switching is triggered by proton motion through inter or intra molecular hydrogen bonds, which play an important role in determining the chemical and electronic mechanism of ferroelectricity.[16–22] The role of the ions carrying permanent dipoles of a polar molecule and orientational ordering of the asymmetric molecules generates spontaneous electric polarization and the reorientation generates ferroelectricity. However, in the paraelectric state, dipoles are reoriented in a disordered manner.[23] Such transformations are known as order–disorder type phase transitions. In the displacive type phase transition, the relative displacement occurs between the charges of the ions yielding microscopic polarization in the crystal (*e.g.* D-sorbose).[24] Several single-component low-molecular-mass compounds such as 4-(4-(methyltliophenyl-2,6-di(1*H*-pyrazol-1-yl)pyridine (UOH1),[25] croconic acid (CRCA),[26] 2-phenylmelondialdehyde,[27] benzimidazoles, some pure organic compounds,[28] α-α-dicyclohexyl-cyclohexane-methanol,[29] 1,3,5-trimethylnitrobenzene,[30] and trisubstituted haloimidazoles,[31] have been investigated for ferroelectricity.

[a] *Solid State and Structural Chemistry Unit, Indian Institute of Science, Bengaluru 560012, India. E-mail: gururow@iisc.ac.in*
[b] *Materials Engineering, Indian Institute of Science, Bengaluru 560012, India*
[c] *Interdisciplinary Centre of Energy Research, Indian Institute of Science, Bengaluru 560012, India*

† Electronic supplementary information (ESI) available: Synthesis, and spectroscopic and structural data of **1–6**. CCDC: 1983772 (**1**), 1983771 (**2**), 1972047 (**3**), 1972046 (**4**), 2305762 (**5**), 2026778 (**6**). For ESI and crystallographic data in CIF or other electronic format see DOI: https://doi.org/10.1039/d3ma01073b

To explore the structure–property relationship of the compounds, special attention has been paid to the variable temperature X-ray crystallography, ferroelectricity and dielectric studies. Particular focus has been put on the understanding of the structure–property relationship, the dynamics of hydrogen bonds and their effects on ferroelectric polarization in these materials. As an important subject of ferroelectrics in classic physics, it is of great potential to incorporate homochirality into ferroelectricity to broaden much more fascinating applications. In organic ferroelectric materials, hydrogen bonds also play an important role in determining the chemical and electronic mechanisms of ferroelectricity. In several small organic ferroelectric materials, the polarization switching is triggered by proton motion within the inter or intra-molecular hydrogen bonds.

Several thermochromic materials have shown that the occurrence of a colour change stems from the onset of a structural phase transition triggered by temperature.[32] Apart from such colour changing phenomena, the temperature induced structural phase transition has also been exploited to realize functional materials with very useful mechanical, electronic, optical, thermal and magnetic properties. Meanwhile, mechanical flexibility, environmental-friendliness, inherent light weight, low acoustical impedance and easy processability, are anticipated to augment the long known thermochromic and ferroelectric field.[33] Additionally, reversible structural phase transitions induced by external stimuli such as temperature, pressure, light, and electromagnetic fields play crucial roles in the solid-state materials for their potential applications in the fields of sensors, actuators, memory devices and security inks.

Herein, we report the synthesis and structure of versatile bend Schiff base derivatives with and without a hydroxyl group at one end acting as an electron donating unit and incorporating oxazolidene-2-one (homochiral group) on the other side acting as an electron acceptor unit. In this context, we have designed room temperature molecular ferroelectrics by including oxazolidinone (homochiral group) into the *N*-benzylideneaniline moiety. The oxazolidinone homochiral group allows the reorientation of the molecules and leads to structural phase transitions. It is generally observed that the change in chirality of the crystals leads to ferroelectric phase transitions and reversal of polarization. Single-component homochiral organic ferroelectric crystals are very rarely reported, although some single component organic ferroelectrics without measurement of Curie temperature (T_c) are reported.[23] Two compounds (*E*)-4-(4(benzylidene amino)benzyl)oxazolidin-2-one (BOA) and (*E*)-4-(4-(2-hydroxybenzylideneamino)benzyl)oxazolidin-2-one (HBOA) (Fig. 1) have been synthesized. The ferroelectric property in these compounds has been confirmed by second harmonic generation (SHG), variable temperature crystal structures, ferroelectric hysteresis loops and anisotropic dielectric measurements. At high temperature, BOA was observed as partially ordered and at room temperature exists as disordered whereas HBOA remains unchanged in the crystal system. Hence the origin of ferroelectricity could be due to order–disorder phase transition in BOA.

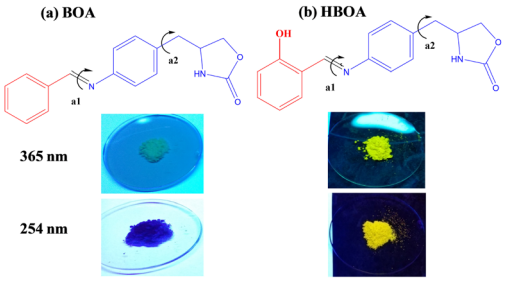

Torsional angles ( )	BOA			HBOA		
	LT	RT	HT	LT	RT	HT
a_1	-179	179	-178	176	-177	-177
a_2	-59	-58	57	-54	56	56

Fig. 1 Molecular structures of propeller shaped and solid emission of BOA and HBOA (as prepared) under UV light irradiation (λ = 254 nm and 365 nm). Torsional angles are represented around the azomethine (–C=N–) bond (a_1) and methylene bond (–CH_2–) (a_2) attached to the chiral centre.

Experimental section

General remarks

Aromatic aldehyde derivatives (H and OH) and 4-(4-aminobenzyl)oxazolidin-2-one were purchased from commercially available sources (Sigma Aldrich and Alfa Aesar, Bengaluru, India) and used without further purification. Solvents (analytical or chromatographic grade) were purchased from local suppliers. Tetrahydrofuran (THF) was distilled under nitrogen before use and used for fluorescence studies. FTIR of BOA and HBOA were recorded on a Bruker Tensor 72, equipped with a diamond cell ATR for the polycrystalline samples obtained by grinding the single crystals. Differential scanning calorimetry (DSC) and thermo gravimetric analysis (TGA) were performed on Mettler Toledo DSC 822e module and Mettler Toledo TGA/SDTA 851e module, respectively. Measurements were carried out over a temperature range of 50–480 °C at a heating rate of 5 °C min^{-1} under a nitrogen atmosphere. Samples were placed in crimped but vented aluminium pans for DSC and open aluminium pans for TGA and purged by a stream of dry nitrogen flowing at 50 mL min^{-1}. DSC peaks were analyzed using STARe (version 8) software and the melting points as well as melt-cool reversibility of single crystal to single crystal transformation of the compounds were evaluated. Powder X-ray diffraction (PXRD) data were measured on a PANalytical X'Pert diffractometer for polycrystalline samples using Cu-Kα X-radiation (λ = 1.54056 Å) operated at 40 kV and 30 mA. An X'Pert High Score Plus (version 1.0d) was used to analyze and plot the diffraction patterns. The PXRD scans were collected in the 2θ range of 5–50° using a step size of 0.013 Å 2θ and time per step of 1 s. All PXRD patterns have been simulated using the coordinates of the respective single crystals obtained from Mercury. Profile fitting refinements were carried out using Jana 2006. Along with the cell dimensions, profile parameters such as GU, GV, GW, LX and LY were refined using the Pseudo-Voigt function. Proton NMR (^{1}H NMR) spectra were recorded on a Bruker 400 MHz spectrometer and Carbon NMR

(^{13}C NMR) on a Bruker 100 MHz spectrometer using d_6 $CDCl_3$ solvent. The well resolved proton spectrum revealed that the characteristics proton (–CH═N–) signals that appear at 8.58 and 8.12 ppm indicate the formation of an azomethine bond in BOA and HBOA, respectively. The hydroxyl proton of HBOA appeared at 12.31 ppm. Absorption and emission spectra were recorded on a PerkinElmer spectrophotometer. Time resolved fluorescence (TRF) data were measured on a FLS920 spectrofluorometer (Edinburg Instruments) using a laser diode for excitation. Dynamic light scattering (DLS) experiments were conducted using a zeta PALS dynamic light scattering particle size analyzer. The surface morphologies were examined with the help of field-emission scanning electron microscopy (Zeiss ultra plus FESEM instrument). The Kurtz and Perry method was utilized to measure the SHG effect on the unsieved powder samples. A Q-switch Nd:YAG laser generated a fundamental wavelength of 1064 nm. Powdered KDP was used as a reference for the measurements. Room temperature and high temperature polarization electric field (PE) loop measurements were carried out using a Precision Premier II tester (Radiant Technologies, Inc.). Heating–cooling dielectric measurements were performed using an Impedance Analyzer (HP 4294A, Agilent Technologies Inc., Santa Clara, CA. Pellets (8 mm in diameter and 1–2 mm thickness) were made by applying 5–8 ton for the ferroelectric and dielectric studies. Pellets were sintered at 130–150 °C for 4–6 h to get maximum density. Subsequently, the samples were coated with silver paste on both sides of the sample and parallel plates were made for behaving as a capacitor. The PFM experiment was carried out in a PARK NX20 AFM instrument. BOA and HBOA are coated on ITO glass using a spin coater (1000 rpm). A 10 μm × 10 μm area containing BOA and HBOA was scanned individually.

Synthesis

Schiff bases BOA and HBOA were synthesized by slowly adding 4-(4-aminobenzyl)oxazolidin-2-one (0.291 g, 1 mmol) and selected aromatic aldehydes (1 mmol) to 10 ml absolute ethyl alcohol using 3–4 drops of glacial acetic acid as a catalyst. The reaction mixture was allowed to reflux at 60–70 °C for 4–5 h (Scheme S1, ESI†) using the reported synthetic methodology.[34] Both compounds were purified by a column using ethylacetate:hexane eluents and recrystallized in methanol by slow evaporation methods. Their molecular structures are shown in Fig. 1 along with their luminescence features in the solid state. Yield of BOA 87% (2.82 g). M.p. 171 °C. FTIR (cm^{-1}): 3370.46 (NH), 3268.72 (–C═H) (Fig. S2, ESI†). ^{1}H NMR ($CDCl_3$): δ 8.58 (s, 1H, ═C–H), 7.88 (S, 1H, NH). ^{13}C NMR ($CDCl_3$): δ 38.21–38.88 (s), 51.55 (m), 67.04 (m), 120.12 (s), 133-135 (s), 148 (s), 157–159 (s) (Fig. S3 and S4, ESI†).

Yield of HBOA 91% (3.02 g). M.p. 184 °C. FTIR (cm^{-1}): 3370.46 (NH), 3268.72 (–C═H) (Fig. S2, ESI†). 1H NMR (CDCl3): δ 12.31 (S, 1H, –OH), 8.12 (s, 1H, ═C–H), 6.97 (S, 1H, NH). 13C NMR (CDCl3): δ 38.31–39.14 (s), 51.73 (m), 67.27 (m), 115.87 (s), 131–134 (s), 145 (s), 157–162 (s) (Fig. S5 and S6, ESI†). HRMS results are shown in (Fig. S7, ESI†) for BOA and HBOA.

Crystallography

Single crystal X-ray diffraction data were collected on an Ultra Smart Apex II at room temperature and low temperature whereas high temperature data were collected on a Bruker Apex II using Mo-Kα radiation (λ = 0.71073 Å). Crystal structures were solved by a direct method with SHELXS-97[35] and refined by full matrix least squares on F2 using SHELXL-97.[36] All non-hydrogen atoms were refined anisotropically. All hydrogen atoms were constrained in geometric positions to their parent atoms. Variable temperature crystallographic data for BOA and HBOA are listed in Tables S1 and S2 (ESI†), respectively.

Thermal properties

The thermal behaviors of BOA and HBOA studied by differential scanning calorimetry (DSC) and thermogravimetric analysis (TGA) are shown in Fig. 2. The DSC and TGA with SDTA thermograms (Fig. 2(a) and (b)) of the polycrystalline samples of BOA and HBOA show a sharp endothermic peak for melting (T_m) at 172.9 °C and 187.11 °C, respectively, and there is no weight loss in the material before their respective melting points. The decomposition temperatures are found to be more than 300 °C, which suggests that the molecules are highly stable. The reversibility of the melt–cool nature of BOA and

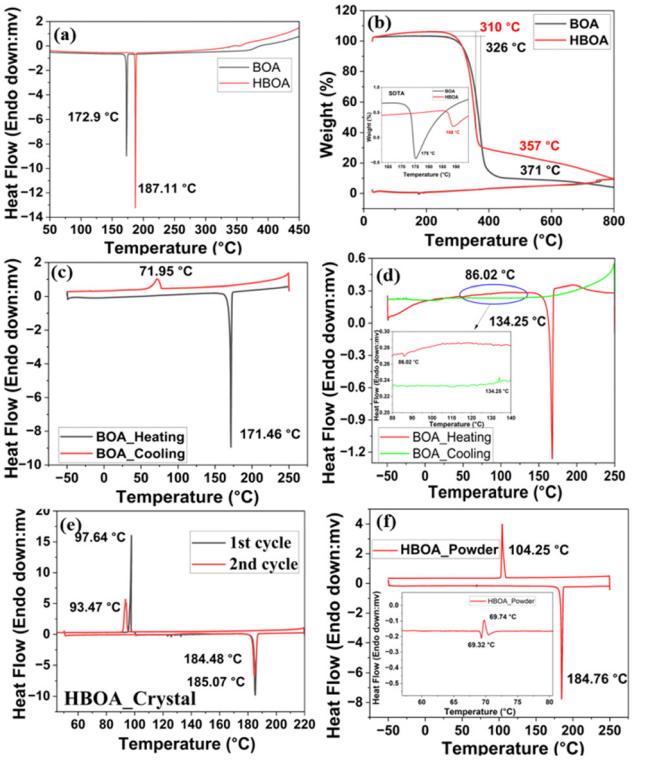

Fig. 2 (a) Differential scanning calorimetry and (b) TGA thermograms of BOA and HBOA. (c) & (d) DSC profile defining the thermal hysteresis in the single crystal and powder sample of BOA, respectively. (e) and (f) DSC profile defining the thermal hysteresis in the single crystal and powder sample of HBOA, respectively. The crystals of BOA and HBOA are shown in the inset.

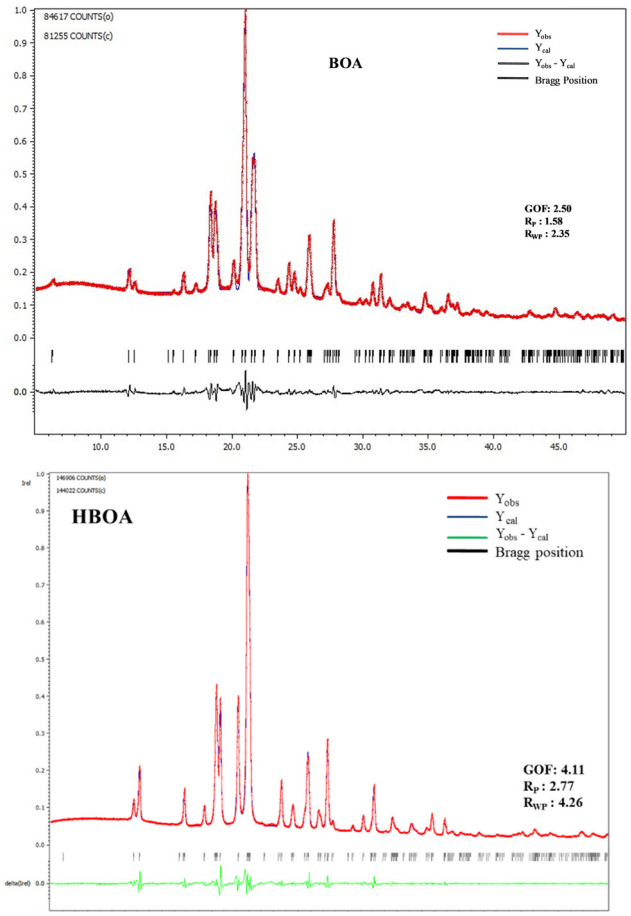

Fig. 3 PXRD pattern of the synthesized sample of BOA and HBOA.

HBOA with respect to temperature change has been observed on their crystals in the temperature range from −50 °C to 250 °C. The heating–cooling thermograms of the crystal and powder sample of BOA are shown in Fig. 2(c) and (d), respectively. Upon the heating–cooling cycle of BOA, an endothermic peak at 171 °C (T_m) and exothermic peak (T_c) at 71 °C are observed, suggesting that the system is reversible with the largest thermal hysteresis of 100 °C (Fig. 2(c)).[37] In the case of HBOA (as shown in Fig. 2(e)), the endothermic and exothermic peaks are at 185 °C and 97 °C, respectively, with a thermal hysteresis of 88 °C. In the second cycle of the heating cooling process, the endothermic and exothermic peaks are regenerated at 184 °C and 93 °C, respectively, with a thermal hysteresis of 91 °C. Very sharp peaks of the DSC curves indicate a first order reversible phase transition with remarkable robustness. Repeated experiments in the powder form of HBOA (shown in Fig. 2(f)), which melts at 184 °C during heating and recrystallized at 104 °C during cooling, confirm a stable large thermal hysteresis of reversible and reproducible nature of the phase transformation. The single crystal (yellow color) of HBOA turns to green after recrystallization (shown in Fig. 2(e)). Enthalpy (ΔH) and entropy (ΔS) were estimated on the basis of DSC results and found to be 2.05; 5.53 and 6.87; 18.5 J K^{-1} respectively.

Table 1 Crystallographic parameters of profile fitting for the synthesized and annealed samples of BOA and HBOA

Empirical formula	BOA	BOA (annealed)	HBOA	HBOA (annealed)
Formula weight	280.30	280.30	296.30	296.30
Wavelength (Å)	1.5418	1.5418	1.5418	1.5418
Space group	$P2_1$	$P2_1$	$P2_1$	$P2_1$
Volume	720.55	720.55	729.33	729.33
Z	2	2	2	2
Density (g cm^{-3})	1.33	1.33	1.35	1.35
R_p	1.58	1.88	2.77	1.66
R_{wp}	2.35	2.58	4.26	2.31
χ^2	2.50	3.25	4.11	3.44

Powder X-ray diffraction analysis

PXRD patterns of the crushed crystals at room temperature were recorded and compared with the simulated patterns from SCXRD data confirming the purity of the samples (Fig. 3). Profile refinement of the PXRD patterns resulted in R_p = 1.58 and 2.77 and R_{wp} = 2.35 and 4.26 for BOA and HBOA, respectively. Crystallographic parameters of BOA and HBOA after profile fitting for the as synthesized and annealed samples are given in Table 1.

Single crystal X-ray diffraction analysis

The single crystal structures of BOA and HBOA adopt 'L' shaped bent molecular structures with both phenyl rings coplanar with the azomethine (–C═N–) bond. Torsional angles (tabulated in Fig. 1) confirm that the 5-membered oxazolidenone ring is distorted from planarity. The oxazolidinone group is highly flexible around the –CH_2–CH– bond and behaves as a ''rotor'' leading to the flip-flop orientation of the oxazolidinone group (Fig. 1). The torsional angles a_1 and a_2 define mutual orientations of the 4-substituted phenyl rings and the methylene group and also characterize the confirmation of the 5-membered oxazolidenone ring. The chirality of the molecules is confirmed by polarimetry. The optical activities of BOA and HBOA are found to be −1.64° and −9.15°, respectively (Tables S3 and S4, ESI†), indicating that the synthesized molecules have a similar conformation to their corresponding precursors. Additionally, the noncentrosymmetric nature of the molecules was confirmed by SHG measurement. BOA and HBOA exhibit nonlinear optical properties with an SHG conversion efficiency of 10 mV and 14 mV, respectively, compared to KDP (standard). Different conformations were analyzed by variable temperature single crystal X-ray diffraction data at 100 K (low temperature, LT), 293 K (room temperature, RT) and 368K (high temperature, HT) for BOA and at 100K (LT), 293 K (RT) and 390K (HT) for HBOA.

Crystal structure of BOA

BOA crystallizes in a monoclinic crystal system with the same space group ($P2_1$) at 100 K (LT), 293 K (RT) and 368 K (HT) containing one molecule in the asymmetric unit with Z = 2. The molecular propagations of BOA at 100 K (LT), 293 K (RT) and 368 K (HT) are shown in Fig. 4(a)–(c). The benzylideneaniline group is twisted from the oxazolidinone group with a torsion

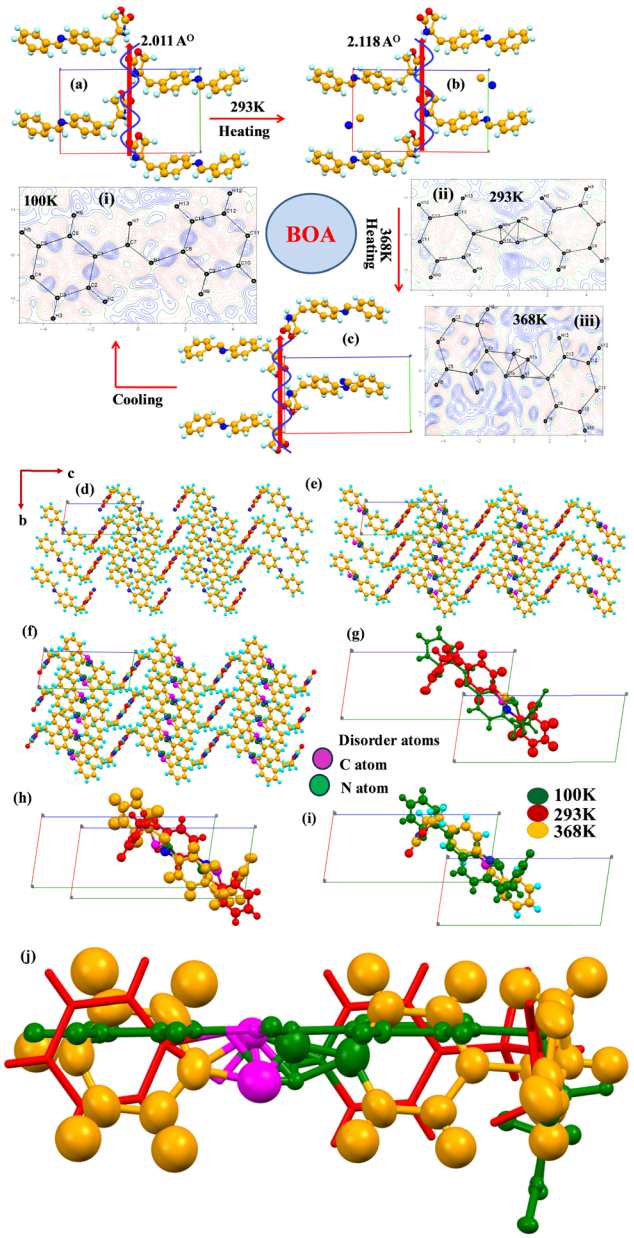

Fig. 4 Molecular propagation diagrams of BOA at (a) 100 K, (b) 293 K and (c) 368 K drawn along the *a*-axis. Difference Fourier maps of BOA are at (i) 100 K, (ii) 293 K and (iii) 368 K. The contour lines are drawn at 0.02 e Å^{-3} intervals. Packing diagrams of BOA at (d) 100 K, (e) 293 K and (f) 368 K drawn with 50% ellipsoid probability. (g) The molecular overlay structures of BOA at 100 K (green) and 293 K (red), in which molecules flip by 180° at 293 K and rotate around –C═N– and –C–C– of the oxazolidin-2-one group at 293 K. (h) The molecular overlay structure of BOA at 293 K (red) and 368 K (orange). (i) The packing overlay structure of BOA at 100 K (green) and 368 K (orange) are the same revealing the reverse back to the original orientation at 368 K. Disordered C and N atoms are represented by Magenta and green colour, respectively, in the packing diagrams. (j) Different confirmations of BOA at 100 K (green), 293 K (red) and 368 K (orange).

angle of 92.82°, 86.15° and 94.49°, whereas the benzylideneaniline and oxazolidinone planes are twisted by 75.15°, 77.46° and 78.35° at LT, RT and HT, respectively. The molecule is found to be ordered at 100 K (LT) (Fig. 4(i)), but observed to be a disordered structure at 293 K (RT) and 368 K (HT). Fourier map analysis reveals that the molecule exhibits dynamic disorder around the azomethine bond (–C═N–) at 293 K and 368 K (Fig. 4(ii) and (iii)). There is electron density left over around the azomethine bond in the Fourier map. The combination of molecular overlay structures at different temperatures (Fig. 4(g)–(i)) reveals that the molecule exhibits molecular dynamics due to flipping and rotation around the azomethine bond as well as the oxazolidenone group, respectively. Minor disordered atoms (C7B and N1B) of the azomethine bond are found to be positioned at the two fold axis and the edges of the unit cell at 293 K, which makes the molecule more polar along the *b* axis. At 368 K, C7B and N1B (minor) atoms are located at the inversion center in the unit cell whereas major C and N atoms are located on the two-fold axis. As the temperature decreases, the C and N atoms return towards an ordered structure. The order–disorder transition of the C and N atoms (which exhibit flip-flop motion by 180° around –C═N–) and the rotation of the oxazolidine-2-one group triggers the molecule to become more polar at room temperature and their atomic displacement governs the ferroelectricity developing along the *b* axis. The molecules propagate in one dimension through a preferred orientation of a strong N–H···O═C hydrogen bond (N···O 2.877(2) Å, 121.87°; 100 K) along the *b* axis through the tail to tail combination, which facilitates the formation of a molecular chain between the nitrogen atom of the amide group of a molecule with the oxygen atom of the keto group of another molecule. Furthermore, the molecules propagate through weak C–H···O (2.491(2) Å, 140.70°; 100 K) and C–H···π (2.655 Å) interactions and form a zig-zag pattern in 3-D along the unique axis represented in Fig. 4(d)–(f). In the 3D structure at 100 K, molecules exist far away from each other at a distance of 6.548 Å and each molecule individually forms N–H···O (N···O 2.877(2) Å, 121.17°) hydrogen bonds with two other molecules. At 293 K, molecules are existing at a distance of 4.371 Å in a tail to tail fashion with a strong hydrogen bond N–H···O (N···O 2.932(2) Å, 120.84°). In the 3D structure, the molecules are packed in a similar tape-like arrangement at 100 K and 368 K whereas at RT the arrangement is found to be J type. Hence the packing structures are different between low temperature and room temperature. The packing overlay arrangement between LT and RT indicates that the origin of the RT cell shifts by 0.75 along the c axis with respect to LT in Fig. 4(g) with 50% overlap of molecules in the LT cell. Therefore, the origin of the RT cell is at the position (0.0, 0.75, 0.0) with respect to the LT cell. C7B and N1B (minor) atoms are also shifted by 0.75 along the a axis from the origin. This suggests that the molecules are freely rotating and have a high degree of reorientation. In the case of RT and HT packing overlay (Fig. 4(h)), the origin of the HT cell is at the position (0.0, 0.50, 0.00) of the RT cell. The temperature-dependent analysis of the molecule suggests that the molecule exhibits molecular dynamics due to order–disorder and displacement of minor atoms in the unit cell. The structural overlay of LT and RT in Fig. 4(i) suggests that the molecule is retrieving its original crystalline state which has

also been confirmed by differential scanning calorimeter analysis.

Crystal structure of HBOA

The HBOA molecule crystallizes in the monoclinic crystal system with space group $P2_1$ with Z = 2 at 100 K, 293 K and 390 K The angle between the long molecular axis and oxazolidene-2-one is 88.78°. Molecules are found to be ordered at all temperatures. The HBOA molecule has a strong intra and two different intermolecular N–H···O bonds at 100 K. The intramolecular hydrogen bond between the oxygen atom of the hydroxyl and the nitrogen atom of azomethine is (N···O; 2.592(2) Å, 86.68°) and the intermolecular N–H···O bond between the NH and oxygen atom of the carbonyl in the amide are (N–H···O; 2.953 (2) Å, 119.69°) and (C═O···H–N; 2.181 (2) Å, 155.64°), respectively. In 2-D, the molecules propagate through both the N–H···O bond and C═O···H–N and form a zig-zag pattern along the *a*-axis (Fig. 5(a)–(c)). Fourier maps of HBOA at different temperatures suggest that there is no electron density left over around the molecule, confirming no disorder in the structure. Temperature induced molecular orientations at different temperatures result in different packing diagrams (Fig. 5(d)–(f)). The molecular overlay suggests that the molecule is highly flexible in nature. The benzylideneaniline group of the molecule is twisted around the methylene bond attached with the oxazolidinone group by a torsion angle of 82.87°, 99.32° and 87.38° whereas the angle between the benzylideneaniline and oxazolidinone planes is 82.68°, 63.07° and 83.45° at LT, RT and HT, respectively (Fig. 5(g)). Apart from that, the hydroxyl phenyl ring also rotates by 179.52° and 99.32° at RT. The overlay structure of LT and RT suggests that the molecule gets oriented by 180° at RT and the unit cell is displaced by 3/4th of that of LT (Fig. 5(h)). The structural overlay between RT and HT in Fig. 5(i) and between LT and HT in Fig. 5(j) suggests that the molecule is oriented by an angle of 60.5° and exists as a scissor with the LT and RT.

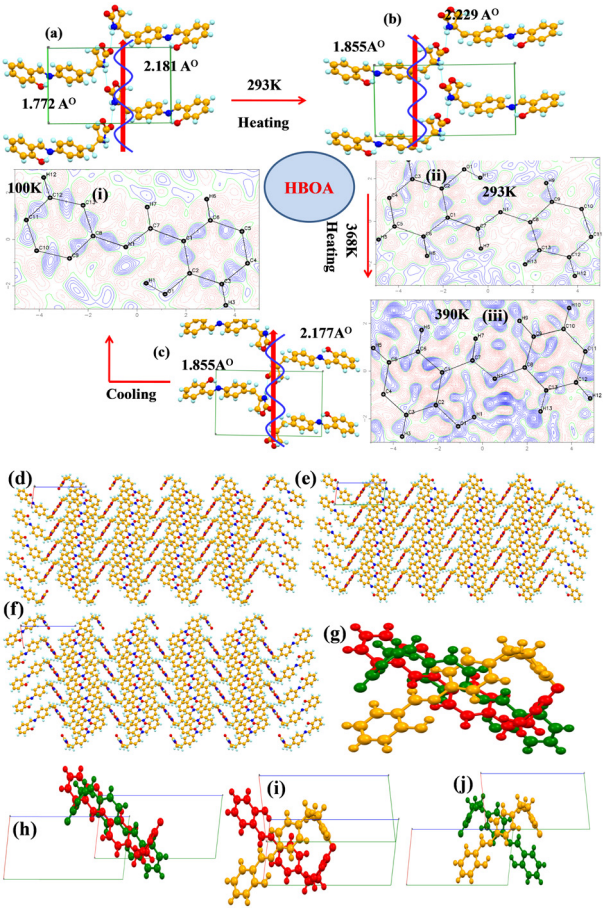

Fig. 5 Molecular propagation diagram of HBOA at (a) 100 K, (b) 293 K and (c) 390 K drawn along the *a*-axis. Difference Fourier maps of HBOA are at (i) 100 K, (ii) 293 K and (iii) 390 K. The contour lines are drawn at 0.02 e Å^{-3} intervals. Packing diagrams of HBOA at (d) 100 K, (e) 293 K and (f) 390 K drawn with 50% ellipsoid probability. (g) The molecular overlay structures of HBOA at 100 K (green), 293 K (red) and 390 K (Orange), in which the molecule flips by 180° at 293 K. At 390 K, the molecule rotates around –C═N– and the methylene bond attached to the oxazolidin-2-one group with an angle of 60.5° exists as scissor-like in the room temperature structure. (h) The molecular overlay structure of HBOA at 100 K (green) and 293 K (red) shows dramatic changes in the structure in the unit cell. Molecules are rotated by 180° at 293 K. (i) The molecular overlay structure of HBOA at 293 K (red) and 390 K (orange). (j) The packing overlay structure of HBOA at 293 K (red) and 390 K (orange).

Mechanofluorochromic (MFC) luminescent behavior of BOA and HBOA

Combining a highly conjugated planar diaryl unit with a non-planar oxazolidine-2-one unit accelerated the accomplishment of prominent solid-state emissive derivatives, which might be responsible for external stimuli. The mechanochromic photoluminescence switching of BOA and HBOA was examined by applying mechanical force using a mortar and pestle. Mechanofluorochromic properties were explored in detail using UV-vis measurements and applying an electric field on pressed pellets. The mechanochromic images are shown in Fig. 6(a). MFC observations were also substantiated by the recording of solid state fluorescence spectra where the corresponding emission maxima were red-shifted from 348 nm to 445 nm on grinding of crystalline BOA and reverted to 350 nm on fuming the ground powder with ethanol, whereas in the case of HBOA, the emission maximum was red-shifted from 530 nm to 610 nm on the grinding of crystalline BOA and reverted to 535 nm on fuming the ground powder with ethanol (Fig. 6(b)). It is concluded that the re-emergence of fluorescence emission upon fumigation is mainly due to the retrieving of its original crystalline state. Furthermore, powder X-ray diffraction (PXRD) measurements were carried out on the pristine crystal, ground crystals, pressed neat pellet and poled pellet to validate the mechanism of mechanofluorochromism (Fig. 7(a) for BOA and Fig. 7(b) for HBOA). Pellets of BOA and HBOA were made by applying hydraulic pressure from 137.90 MPa to 165.47 MPa using a pressure gauge. Poled states of BOA and HBOA are achieved under a DC field of 5 kV cm^{-1} and 8 kV cm^{-1}, respectively, in a silicon oil bath at room temperature for 45 min.

The diffraction patterns of BOA and HBOA display intense and sharp peaks that suggest that the pristine sample is in a

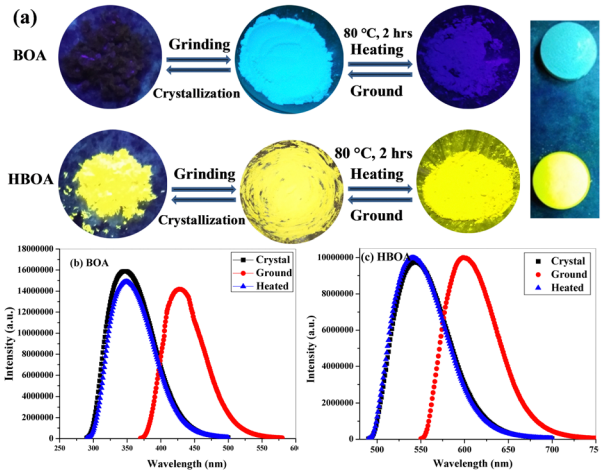

Fig. 6 (a) Mechanochromic photoluminescence images of the pristine and ground powder before and after heating and fumed samples of BOA and HBOA. (b) PL spectra of the crystals, ground and fumed samples of BOA and (c) PL spectra of the crystals, ground and fumed samples of HBOA.

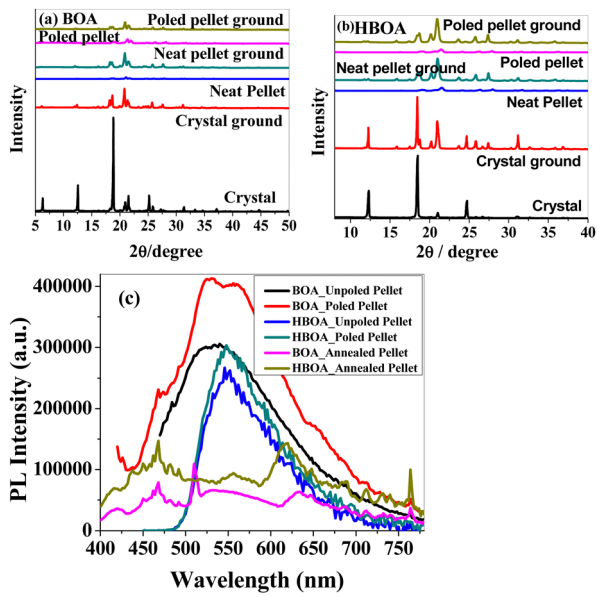

Fig. 7 PXRD pattern of the pristine crystal, pristine crystal ground, neat pellet, neat pellet ground, poled pellet and poled pellet ground of (a) BOA and (b) HBOA, and (c) PL of unpoled, poled and annealed pellets of BOA and HBOA.

well-ordered crystalline state. In the ground samples of BOA and HBOA, less intense peaks are observed indicating semi-crystalline nature. A further decrease in intensity and change in peak position was observed in the neat pellet and poled pellet for a few peaks showing some structural changes, but revert to the ground neat pellet and ground poled pellet. These observations demonstrate that the mechanofluorochromism of BOA and HBOA is reversible upon grinding and annealing treatments.[38,39] These results strongly suggested the nonplanar structure of the molecules and loose molecular packing of the compounds.

Morphological study

Scanning emission microscopy (SEM) studies were carried out to analyze the morphological and structural properties of the poled and unpoled samples of BOA and HBOA (Fig. 8). The surface morphologies of BOA and HBOA are sharp crystalline plates that are well matched with the single crystal structures. The particle sizes found to be less than 300 nm were also absorbed, which group to form agglomerates of larger size. Powder samples of BOA consisting of particles with a size between 100 nm and 280 nm showed a transition from irregular to a round shape. For BOA, the EDAX results of unpoled and poled samples showed that the atomic percentages of carbon, nitrogen and oxygen are 69.01, 9.60, 21.40 and 74.60, 9.20, 16.19%, respectively, whereas for HBOA, the EDAX results of unpoled and poled sample showed that the atomic percentages of carbon, nitrogen and oxygen are 74.31, 6.71, 18.98 and 75.72, 4.91, 19.37%, respectively.[40]

Quantum chemical calculations of BOA

The molecular geometry of BOA was optimized and the HOMO–LUMO energy values were determined by the Gaussian 09 program using the DFT/B3LYP/6-31G* method[41] and depicted in Fig. 9. The HOMO–LUMO orbitals play a vital role in understanding the electronic structures and transitions due to the electron donating and accepting abilities. A low value of the energy gap suggests that the molecules are more reactive, soft and have easier π–π* electronic transitions. The HOMO orbitals of BOA are localized in the phenyl and azomethine bond, whereas the LUMO orbitals are located in the benzylideneaniline ring. According to Mulliken charge density, the electron density of the nitrogen atom (−0.4492) of the oxazolidinone group is more than that of the oxygen atom (−0.5985) of the

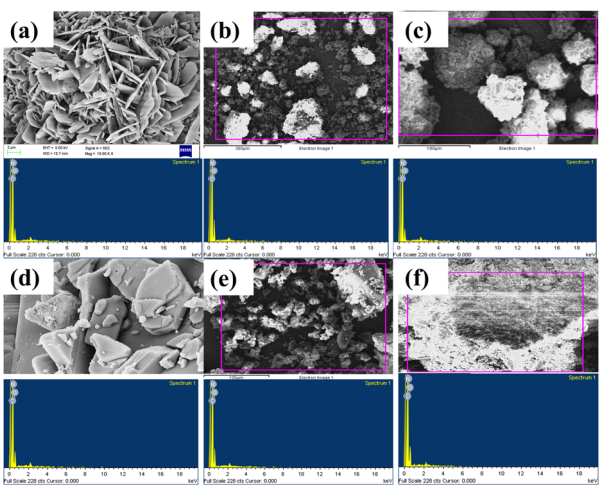

Fig. 8 (a) Crystalline, (b) unpoled and (c) poled SEM images of BOA. (d) Crystalline, (e) unpoled and (f) poled SEM images of HBOA. EDAX photographs (shown in blue colour) of BOA and HBOA are presented below their corresponding SEM images.

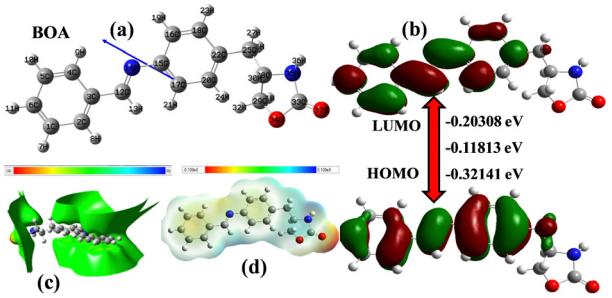

Fig. 9 (a) Optimized structure and (b) counter plots of the electron density distribution and energy values of HOMO/LUMO, (c) TED and (d) ESP of BOA by DFT calculation.

carbonyl group. Thus, charge transfer occurs from the nitrogen atom to the carbonyl group. Absorption peaks were observed at 360 nm and 270 nm, in which the first peak may be due to the transition of one electron from the HOMO to LUMO (π–π* transition), whereas the second peak represents both the n–π* and π–π* transitions.

Room temperature and temperature dependent ferroelectric and dielectric studies

The ferroelectric properties of BOA and HBOA were studied in pressed pellet and crystal form, respectively. Room temperature and temperature dependent *P–E* loops were investigated and traced out the electric polarization *versus* electric field. This experiment revealed that the hysteresis loops of BOA gradually increase upon increasing the applied voltage at a frequency of 1 Hz.[42] The maximum breakdown electric field and coercive field for polarization reversal were observed to be extremely high due to the rotation of the oxazolidene-2-one group associated with the main chain resulting in it withstanding up to 140 kV cm^{-1} at 1 Hz.[42] The *P–E* loop reaches its saturation with a saturation polarization of P_{ME} = 139.7132 μC cm^{-2}, P_r = 0.5248 μC cm^{-2} and E_c = 91.0065 kV cm^{-1}. The electric field tolerated up to 181 kV cm^{-1} (Instrumentation limit) at 2 Hz. The major aim was to find the maximum breakdown electric field and phase transition temperature by analyzing the electric field and temperature-dependent bipolar hysteresis *P–E* loops.[43] The temperature dependent *P–E* hysteresis loops of BOA were recorded at an electric field of 135 kV cm^{-1} and a frequency of 1 Hz by varying the temperature from 30 °C to 75 °C and used to interpret the relation of remnant polarization (P_r), polarization maximum electric field (P_{ME}) and coercive field (E_c) with electric field. The results (shown in Fig. 10) revealed that with the increase in temperature, the PE hysteresis loop increases due to an increase in energy dissipation confirming the leaky nature of the material.[44] Energy dissipation is responsible for the separation of charge and voltage signals resulting in a considerable increment in the area of the PE loops.[45] The area of a PE loop defines the charge storage ability of the material. The greater the area of a loop, the greater the charge ability of the material.[46] This is possible due to a change in molecular orientation, which is also confirmed by the single crystal data analysis. A sudden change was observed

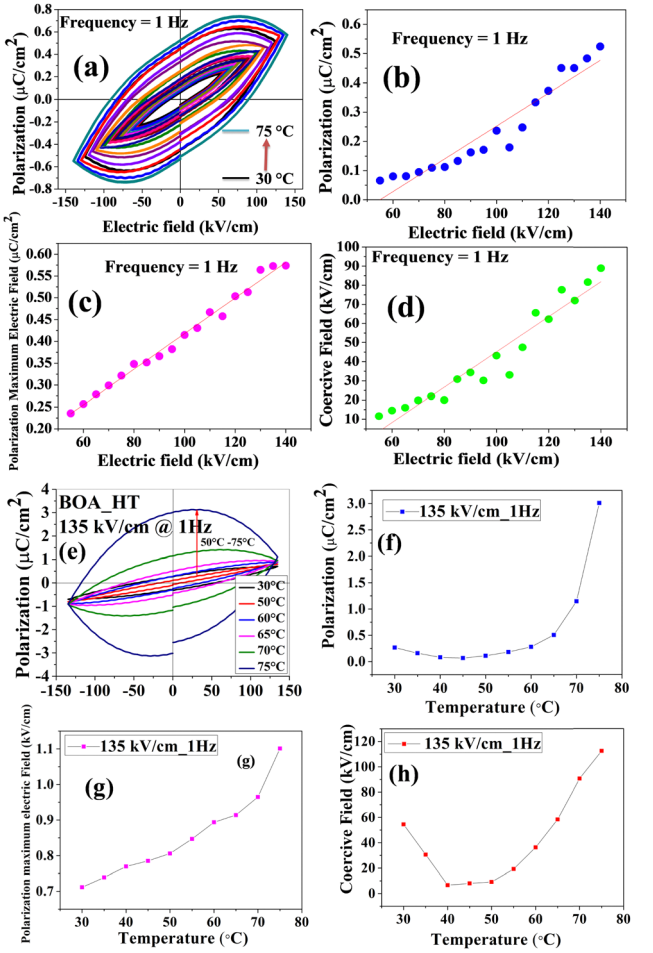

Fig. 10 (a) Room temperature bipolar polarization hysteresis loops of the BOA on a pressed pellet at 1 Hz. (b)–(d) Correlation of remnant polarization (P_r), polarization maximum electric field (P_{ME}) and coercive field (E_c) with an electric field at 1 Hz. (e) Temperature-dependent *P–E* loops of BOA at 135 kV cm^{-1}. (f)–(h) Temperature dependent polarization (P_r), polarization maximum electric field (P_{ME}) and coercive field (E_c) at 135 kV cm^{-1}, respectively.

in the range of 65–75 °C, which indicates that a phase transition occurred in this temperature range. The collective data single crystal analysis, thermal and ferroelectric hysteresis evidenced that the single molecule behaves as a proper ferroelectric rather than a relaxor one and undergoes an order–disorder ferroelectric phase transition at the Curie temperature (T_c = 71.95 °C (345 K)).

The variation trends of temperature-dependent P_r, E_c and P_{ME} are in good accordance with the phase transition deduced from single crystal XRD and dielectric analysis. The origin of the ferroelectricity and switching behavior can be induced by proton transfer[47,48] and changing the molecular orientation of the crystal components (Fig. 11).[49–51] Another reason could be the displacement of C7B and N1B suggests the order–disorder behaviors of minor atoms and displacement of the unit cell in the BOA molecule. The ferroelectric hysteresis loop of HBOA was measured in a single crystal (Fig. 11) and the results revealed imperfect switching, which arises due to the charged

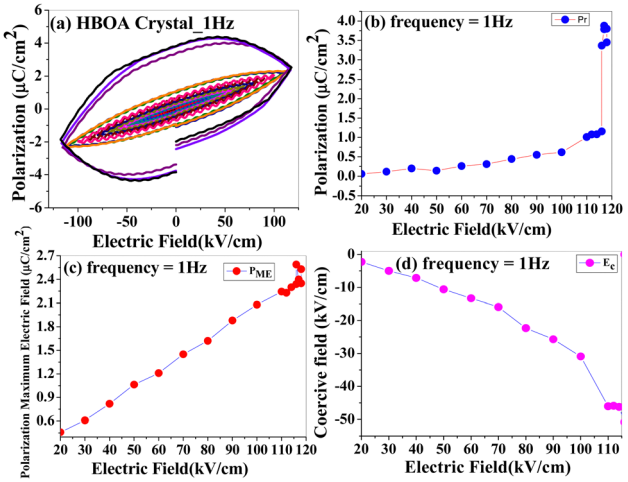

Fig. 11 (a) Room temperature bipolar polarization hysteresis loops of the HBOA on the crystal at 1 Hz. (b)–(d) Correlation of remnant polarization (P_r), polarization maximum electric field (P_{ME}) and coercive field (E_c) with an electric field at 1 Hz.

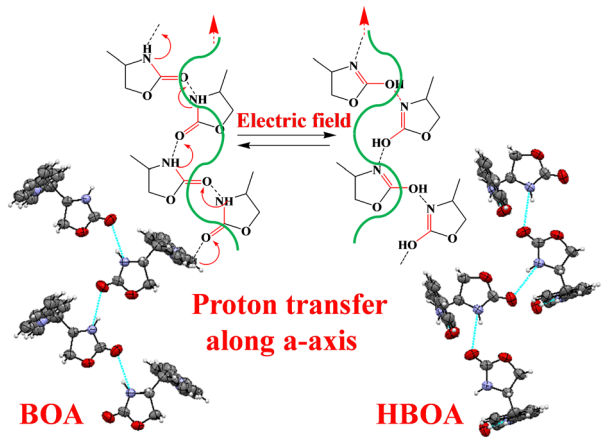

Fig. 12 The crystal polarity can be inverted by proton transfer over a hydrogen bond and simultaneous interconversion of the single and double bonds, which are specified in red. The dotted lines indicate the proton transfer paths over the intermolecular N–H···O hydrogen bonds. The thick arrow indicates the electric polarity of each hydrogen-bonded chain.

domain walls of the multidomain crystal. The *P*–*E* loop reaches its saturation with a saturation polarization of P_{ME} = 2.5304 μC cm^{-2}, P_r = 3.8855 μC cm^{-2} and E_c = 98.2695 kV cm^{-1}.

An interesting result was observed that both the molecules are able to withstand very high electric fields up to 181 kV cm^{-1} (Instrumentation limit) compared with other ferroelectric organic molecules. Horiuchi *et al.* worked on croconic acid at 37 kV cm^{-1}; Kamishina *et al.* investigated trichloroacetamide at 7.5 kV cm^{-1}, Venkataramudu *et al.* studied 4-(4-(methylthio)-phenyl)-2,6-di(1*H*-pyrazol-1-yl)pyridine (UOH1) at 140 kV cm^{-1}, and Bauer and Dormann studied substituted diacetylene l,6-bis(2,4-dinitrophenoxy)-2,4-hexadiyne (DNP) at 33 kV cm^{-1}.[16,52–54]

The crystal structure of BOA and HBOA is extended in a one-dimensional network through N–H···O═ bonds (Fig. 12). The polarity of the hydrogen-bonded networks is switchable through cooperative proton transfer and concomitant interchange of double and single-bond locations.[55] In addition, a hidden pseudosymmetry survives as a paraelectric configuration in HBOA. In the case of HBOA, single crystal analysis indicated a displacement of the unit cell along the *c*-axis by $\frac{1}{4}$ of the unit cell at RT. The N–H···O hydrogen bonds form spiral bands running along the *b* axis.

PUND (positive up and negative down) studies

PUND study is the most convincing proof of the ferroelectricity for ferroelectric materials. In PUND studies, the switchable polarization is isolated from non-switchable (*i.e.* non-remanant) polarization by applying a series of five pulses (one preset and two positive up and two negative down), which measures different polarizations. The difference in polarization value in the two cases gives the value of true switchable polarizations.[56,57] PUND analysis (Fig. 13) was performed (using Radiant ferroelectricity tester) on the pellet of BOA and single crystal of HBOA (as in Fig. 13(a), (c) and (b), (d), respectively, which clearly shows that both compounds possess

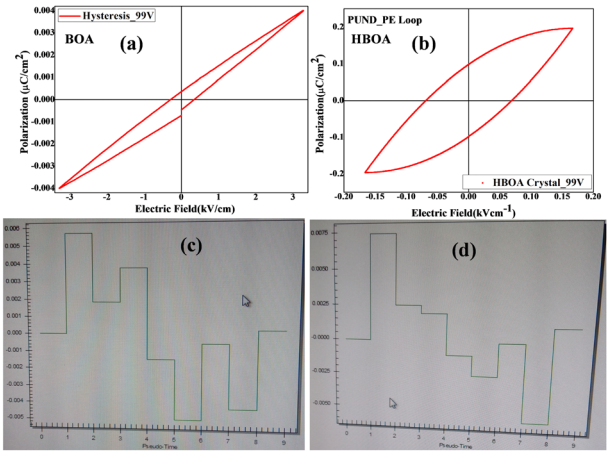

Fig. 13 PUND data collected at an electric field of 99 V cm^{-1}, pulse width of 650 ms and pulse delay of 1000 ms for BOA and HBOA. (a) and (b) Hysteresis loop and switching polarization of BOA in the pellet. (c) and (d) Hysteresis loop and switching polarization of HBOA in the crystal.

a switching polarization component and hence established ferroelectricity in the sample, despite having an unsaturated *P*–*E* loop. Thus, we can conclude that merely the failure of attaining a saturated *P*–*E* loop due to measurement at low

Table 2 PUND parameters for BOA and HBOA

Polarization values	BOA	HBOA
P^* (μC cm^{-2})	3.300	4.652
P_r^* (μC cm^{-2})	2.588	2.904
$P^\wedge$ (μC cm^{-2})	3.442	4.785
$P_r^\wedge$ (μC cm^{-2})	2.744	3.033
$-P^*$ (μC cm^{-2})	1.986	0.997
$-P_r^*$ (μC cm^{-2})	2.728	2.844
$-P^\wedge$ (μC cm^{-2})	2.165	1.167
$-P_r^\wedge$ (μC cm^{-2})	2.948	3.040

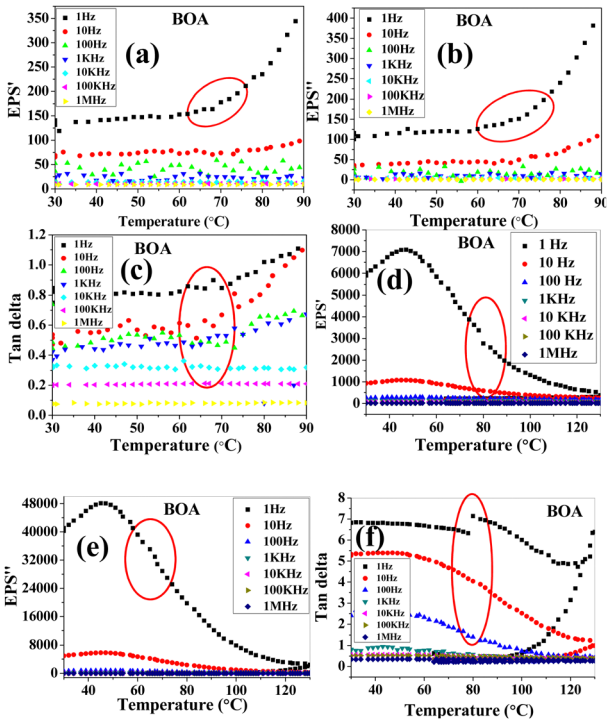

Fig. 14 Temperature dependence of the (a) dielectric constant, and (b) imaginary and (c) loss tangent of BOA. Heating–cooling dielectric plots of (d) dielectric constant, and (e) imaginary and (f) loss tangent of BOA.

electric field is not sufficient to conclude the non-existence of ferroelectricity in the samples.

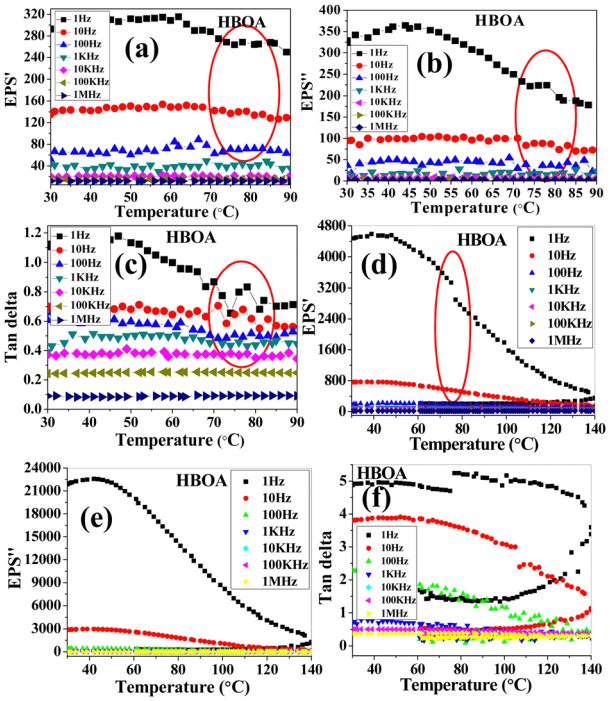

Fig. 15 Temperature dependence of the (a) dielectric constant, and (b) imaginary and (c) loss tangent of HBOA. Heating–cooling dielectric plots of (d) dielectric constant, and (e) imaginary and (f) loss tangent of HBOA.

In the Radiant PUND experiment, only a single polarization measurement is executed at the top of each pulse and the bottom of each pulse, yielding eight polarization quantities. Data is given in Table 2 below.

Dielectric properties of BOA and HBOA

The temperature dependent dielectric properties were studied over a range of frequencies from 1 Hz to 1 MHz using a precision LC meter. Before measurements, pressed pellets of BOA and HBOA were annealed for 4–6 h at 130 °C and 140 °C, respectively. Measurement was done at a rate of 5 °C from 30 °C to 130 °C for BOA and 30 °C to 140 °C for HBOA. Temperature dependence of the dielectric constant (EPS′ (real), EPS″ (imaginary)) and Tan delta parts of BOA and HBOA are shown in Fig. 14 and 15, respectively.

The real part of the dielectric permittivity of BOA shows a change at 70 °C, which is consistent with the structural changes observed from the single crystal diffraction and DSC data. The EPS′ value of 160 was observed at 70 °C at a frequency of 1 Hz. The transition point of HBOA was beyond the measurement. High dielectric constant was observed for BOA and HBOA compared to other non-ionic organic molecules to date.[58,59] It is found that with the increase in temperature, the dielectric loss increases. The mobility of the charge carriers increases

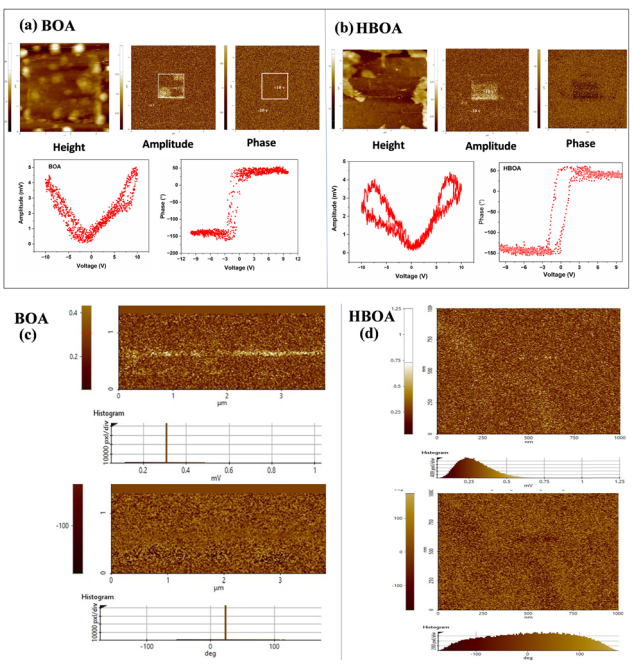

Fig. 16 Vertical images of piezoresponse force microscopy (PFM) of BOA and HBOA. In (a) and (b) Topography, amplitude contrast, phase contrast at +10 V and −10 V, PFM phase voltage hysteresis loop and amplitude voltage butterfly loop suggesting a uniform piezoelectric force response as a function of DC bias of BOA and HBOA, respectively.[64,65] (c) and (d) Piezoelectric force microscopy images (left: amplitude contrast; right: phase contrast) of surface morphology for the epitaxial (a) BOA and (b) HBOA film, respectively. The images were recorded at a bias of ±10 V in a 3.8 × 3.8 μm^2 area. Histograms plots are shown below of the contrast images for BOA and HBOA.

with temperature leading to an increase in polarization and dielectric loss. The maximum value of dielectric constant decreases sharply with increasing frequencies indicating the greater contribution of dipolar and space charge distribution in the systems.[60] The change in dielectric permittivity and Tan delta during the heating–cooling cycle at 70 °C is due to the noncooperative motion of dipoles with the electric fields, which enhances space charge and dipolar polarization.[61–63]

PFM characterization of BOA and HBOA

The piezoelectricity of BOA and HBOA was characterized by the PFM method. The amplitude image shows a strong piezoelectric contrast because of the deflection caused by the ±10 V applied field shown in Fig. 16(a) and (b). The PFM phase voltage hysteresis loop and amplitude voltage butterfly loop suggest a uniform piezoelectric force response as a function of DC bias of BOA and HBOA, respectively. The phase images of BOA and HBOA clearly display both negative and positive values indicating antiparallel ferroelectric 180° surface morphology (Fig. 16(c) and (d) for BOA and HBOA, respectively).

Conclusions

BOA and HBOA molecules are synthesized and a significant thermal hysteresis of reversible single crystal to single crystal transformation is observed with temperature in both the molecules. SHG measurements verify that the compounds are noncentric and mechanofluorochromic (MFC) experiments confirm the reversible nature of these compounds. Additionally, the tolerance to high electric field (up to 181 kV cm^{-1}) without any breakdown will be a beneficial factor to consider in the design of thermochromic materials. The existence of an explicit V_c in PFM measurement is proposed as an important approach to unambiguously identify intrinsic ferroelectricity in materials. Thus, these new series of compounds would be suitable for the futuristic design of switchable memory devices.

Abbreviations

SCSC	single crystal to single crystal
DSC	differential scanning calorimetry
PUND	positive up and negative down
LT	low temperature
RT	room temperature
HT	high temperature
PXRD	powder X-ray diffraction

Conflicts of interest

There are no conflicts to declare.

Acknowledgements

We thank Prof. Rajeev Ranjan, Department of Material Engineering for providing instrumental facilities for ferroelectric and dielectric measurements. We thank Prof. S. Elizabeth Saji for the PUND measurements. We also thank Prof. Pushpendu K. Das and Prof. Partha Sarathi Mukherjee from Department of Inorganic and Physical Chemistry, IISc, for providing instrumental facilities. AD is thankful for an Inspire Fellowship, Department of Science and Technology (DST), Government of India (GOI). AJB acknowledges DST/TMD/MECSP (2017/07), SERB-IRPHA (IPA/2021/000007), and JC Bose Fellowship, GOI (JCB/2022/000016) for research funding. TNG thanks INSA and RK thanks to DST/INT/DFG/P-04/2021 & 31/03/2021.

References

1 J. F. Scott, Applications of Modern Ferroelectrics, *Science*, 2007, **315**, 954–959.
2 P. F. Li, Y. Y. Tang, Z. X. Wang, H. Y. Ye, Y. M. You and R. G. Xiong, Anomalously rotary polarization discovered in homochiral organic ferroelectrics, *Nat. Commun.*, 2016, **7**, 13635.
3 Z. Sun, Y. Tang, S. Zhang, C. Ji, T. Chen and J. Luo, Ultrahigh Pyroelectric Figures of Merit Associated with Distinct Bistable Dielectric Phase Transition in a New Molecular Compound: Di-n-Butylaminium Trifluoroacetate, *Adv. Mater.*, 2015, **27**, 4795–4801.
4 P. Jain, N. S. Dalal, B. H. Toby, H. W. Kroto and A. K. Cheetham, Order−Disorder Antiferroelectric Phase Transition in a Hybrid Inorganic−Organic Framework with the Perovskite Architecture, *J. Am. Chem. Soc.*, 2008, **130**, 10450.
5 W. Zhang, H. Y. Ye, R. Graf, H. W. Spiess, Y. F. Yao, R. Q. Zhu and R. G. Xiong, Tunable and Switchable Dielectric Constant in an Amphidynamic Crystal, *J. Am. Chem. Soc.*, 2013, **135**, 5230–5233.
6 Y. Zhang, H. Y. Ye, H. L. Cai, D. W. Fu, Q. Ye, W. Zhang, Q. Zhou, J. Wang, G. L. Yuan and R. G. Xiong, Switchable Dielectric, Piezoelectric, and Second-Harmonic Generation Bistability in a New Improper Ferroelectric above Room Temperature, *Adv. Mater.*, 2014, **26**, 4515–4520.
7 J. P. Zhao, J. Xu, S. D. Han, Q. L. Wang, X. H. Bu and A. Niccolite, Structural Multiferroic Metal–Organic Framework Possessing Four Different Types of Bistability in Response to Dielectric and Magnetic Modulation, *Adv. Mater.*, 2017, **29**, 1606966.
8 C. Shi, X. Zhang, Y. Cai, Y. F. Yao and W. Zhang, A chemically triggered and thermally switched dielectric constant transition in a metal cyanide based crystal, *Angew. Chem., Int. Ed.*, 2015, **54**, 6206–6210.
9 P. Meng, Q. Zhang, Y. L. Wu, Z. Y. Tan, G. A. Cheng, X. L. Wu and R. T. Zheng, Room-Temperature Dielectric Switchable Nanocomposites, *Adv. Funct. Mater.*, 2017, **27**, 1701136–1701143.
10 M. Owczarek, K. A. Hujsak, D. P. Ferris, A. Prokofjevs, I. Majerz, P. Szklarz, H. Zhang, A. A. Sarjeant, C. L. Stern, R. Jakubas, S. Hong, V. P. Dravid and J. F. Stoddart, Flexible

ferroelectric organic crystals, *Nat. Commun.*, 2016, **7**, 13108–13118.
11 O. Sato, Dynamic molecular crystals with switchable physical properties, *Nat. Chem.*, 2016, **8**, 644–656.
12 M. Irie, T. Fukaminato, K. Matsuda and S. Kobatake, Photochromism of Diarylethene Molecules and Crystals: Memories, Switches, and Actuators, *Chem. Rev.*, 2014, **114**, 12174–12277.
13 C. S. Vogelsberg and M. A. Garcia-Garibay, Crystalline molecular machines: function, phase order, dimensionality, and composition, *Chem. Soc. Rev.*, 2012, **41**, 1892–1910.
14 W. Fujita, Awaga, Kunio, Room-Temperature Magnetic Bistability in Organic Radical Crystals, *Science*, 1999, **286**, 261–263.
15 Z. S. Yao and T. J. Tao, Bistable molecular materials with dynamic structures, *Chem. Commun.*, 2020, **56**, 2071–2080.
16 S. Horiuchi, Y. Tokunaga, G. Giovannetti, S. Picozzi, H. Itoh, R. Shimano, R. Kumai and Y. Tokura, Above-room-temperature ferroelectricity in a single-component molecular crystal, *Nature*, 2010, **463**, 789–792.
17 S. Horiuchi, F. Kagawa, K. Hatahara, K. Kobayashi, R. Kumai, Y. Murakami and Y. Tokura, Above-room-temperature ferroelectricity and antiferroelectricity in benzimidazoles, *Nat. Commun.*, 2012, **3**, 1308.
18 S. Horiuchi, K. Kobayashi, R. Kumai and S. Ishibashi, Proton tautomerism for strong polarization switching, *Nat. Commun.*, 2017, **8**, 14426.
19 S. Horiuchi, R. Kumai and Y. Tokura, Hydrogen-Bonding Molecular Chains for High-Temperature Ferroelectricity, *Adv. Mater.*, 2011, **23**, 2098–2103.
20 S. Horiuchi and S. Ishibashi, Hydrogen-Bonded Small-Molecular Crystals Yielding Strong Ferroelectric and Antiferroelectric Polarizations, *J. Phys. Soc. Jpn.*, 2020, **89**, 051009.
21 S. Horiuchi, S. Ishibashi, S. Inada and S. Aoyagi, Hydrogen-Bonded Architectures and Field-Induced Polarization Switching in Bridged Bis(benzimidazole) Crystals, *Cryst. Growth Des.*, 2019, **19**(1), 328–335.
22 S. Dutta, K. Vikas, A. Yadav, R. Boomishankar, A. Bala, V. Kumar, T. Chakraborty, S. Elizabeth and P. Munshi, Record-high thermal stability achieved in a novel single-component all-organic ferroelectric crystal exhibiting polymorphism, *Chem. Commun.*, 2019, **55**, 9610–9613.
23 S. Horiuchi and Y. Tokura, Organic ferroelectrics, *Nat. Mater.*, 2008, **7**, 357–366.
24 S. Iwagaki, H. Kakuta, Y. Yamamura, H. Saitoh, M. Hishida, K. Fukada and K. Saito, Ordering Phase Transition with Symmetry-Breaking from Disorder over Non-Equivalent Sites: Calorimetric and Crystallographic Study of Crystalline D-Sorbose, *Crystals*, 2020, **10**, 361.
25 U. Venkataramudu, C. Sahoo, S. Leelashree, M. Venkatesh, D. Ganesh, S. R. G. Naraharisetty, A. K. Chaudhary, S. Srinath and R. Chandrasekhar, *J. Mater. Chem. C*, 2018, **6**, 9330–9335.
26 S. Mohapatra, V. D. Costa, G. Avedissian, J. Arabski, W. Weber, M. Bowen and S. Boukari, Robust ferroelectric properties of organic croconic acid films grown on spintronically relevant substrates, *Adv. Mater.*, 2020, **1**, 415–420.
27 W. Guan, N. Kida1, M. Sotome, Y. Kinoshita, R. Takeda, A. Inoue, S. Horiuchi and H. Okamoto, Terahertz radiation by optical rectification in a hydrogen-bonded organic molecular ferroelectric crystal, 2-phenylmalondialdehyde, *Jpn. J. Appl. Phys.*, 2014, **53**, 09PD07.
28 R. R. Choudhary and R. Chitra, Molecular symmetry and ferroelectricity in pure organic molecular crystals, *Cryst. Res. Technol.*, 2006, **41**(10), 1045–1048.
29 G. Bator1, R. Jakubas1 and Z. Malarski1, Molecular dynamics in the α-α-dicyclohexyl-cyclohexane-methanol single crystal ((C6H11)3COH), *Phys. C: Solid State Phys.*, 1986, **19**, 2799.
30 P. Szklarz, V. Kinzhybalo and G. Bator, Ferroelectricity and switching polarization on the C–H···π bond in a pure organic molecular crystal – 1,3,5-trimethylnitrobenzene, *CrystEngComm*, 2021, **23**, 4005–4012.
31 M. Owczarek, K. A. Hujsak, D. P. Ferris, A. Prokofjevs, I. Majerz, P. Szklarz, H. Zhang, A. A. Sarjeant, C. L. Stern, R. Jakubas, S. Hong, V. P. Dravid and J. F. Stoddart, Flexible ferroelectric organic crystals, *Nat. Commun.*, 2016, **7**, 13108.
32 P. Kiri, G. Hyett and R. Bininons, Solid state thermochromic materials, *Adv. Matter. Lett.*, 2010, **1**(2), 86–105.
33 J. C. Liu, W. Q. Liao, P. F. Li, Y. Y. Tang, X. G. Chen, X. J. Song, H. Y. Zhang, Y. Zhang, Y. M. You and R. G. Xiong, A molecular thermochromic ferroelectric, *Angew. Chem., Int. Ed.*, 2020, **59**(9), 3495–3499.
34 M. M. Y. Kuddushi, M. A. H. Malek, L. Vinod, P. M. S. Patel, R. K. Patel and R. H. Dave, Synthesis and characterization of Schiff base aniline with 5-bromo -2- hydroxyl benzaldehyde and their metal complexes, *Int. J. Recent Sci. Res.*, 2018, **9**(4), 26026–26030.
35 G. M. Sheldrick, Phase annealing in SHELX-90: Direct methods for larger tructures, *Acta Crystallogr., Sect. A: Found. Crystallogr.*, 1990, **A46**, 467.
36 G. M. Sheldrick, *Program for Crystal Structure Solution and Refinement. SHELXL-97*, Universitat Gottingen, Gottingen, 1997.
37 C. Lochenie, W. Bauer, A. P. Railliet, S. Schlamp, Y. Garcia and B. Weber, Large Thermal Hysteresis for Iron(II) Spin Crossover Complexes with N-(Pyrid-4-yl)isonicotinamide, *Inorg. Chem.*, 2014, **53**(21), 11563–11572.
38 Y. Y. Gong, Y. R. Zhang, W. Z. Yuan, J. Z. Sun and Y. M. Zhang, D–A Solid Emitter with Crowded and Remarkably Twisted Conformations Exhibiting Multifunctionality and Multicolor Mechanochromism, *J. Phys. Chem. C*, 2014, **118**, 10998–11005.
39 S. S. Pasha, H. R. Yadav, A. R. Choudhury and I. R. Laskar, Synthesis of an aggregation-induced emission (AIE) active salicylaldehyde based Schiff base: study of mechanoluminescence and sensitive Zn (ii) sensing, *J. Mater. Chem. C*, 2017, **5**, 9651–9658.
40 S. D. Vacche, D. Damjanovic and V. Michaud, Leterrier, Yves. Interface-Dominated Time-Dependent Behavior of Poled Poly(Vinylidene Fluoride–Trifluoroethylene)/Barium Titanate Composites, *Materials*, 2020, **13**(1), 225–239.

41 A. D. Becke, Density-functional thermochemistry. III. The role of exact exchange, *J. Chem. Phys.*, 1993, **98**, 5648–5653.
42 H. Barhum, C. McDonnell, T. Alon, R. Hammad, M. Attrash, T. Ellenbogen and P. Ginzburg, Organic Kainate Single Crystals for Second-Harmonic and Broadband THz Generation, *ACS Appl. Mater. Interfaces*, 2023, **15**(6), 8590–8600.
43 M. N. Al-Aaraji1, W. N. Hasan and K. Al-Marzoki, Progress In Lead Free- Relaxor Ferroelectrics For Energy Storage Applications, *J. Phys.: Conf. Ser.*, 2021, **1973**, 012117.
44 A. Durán, H. Tiznado, J. M. R. Herrera, D. Domínguez, R. Escudero and J. M. Siqueiros, Nanocomposite YCrO3/Al2O3: Characterization of the Core–Shell, Magnetic Properties, and Enhancement of Dielectric Properties, *Inorg. Chem.*, 2014, **53**(10), 4872–4880.
45 S. Horiuchi, R. Kumai and Y. Tokura, Hydrogen-bonded donor–acceptor compounds for organic ferroelectric materials, *Chem. Commun.*, 2007, 2321–2329.
46 W. He, Q. Li, Q. Yan, N. Luo, Y. Zhang, X. Chu and D. Shen, Temperature-dependent phase transition in orthorhombic [011]C Pb(Mg1/3Nb2/3)O3–0.35PbTiO3 single crystal'', *Crystals*, 2014, **4**(3), 262–272.
47 R. N. Perumal and A. Marimuthu, Temperature dependence on dielectric and ferroelectric properties of rubidium titanyl phosphate single crystal, *J. Mater. Sci.: Mater. Electron.*, 2020, **31**, 6385–6393.
48 D. K. Pradhan, B. K. Samantaray, R. N. P. Choudhary and A. Thakur, Complex impedance analysis of layered perovskite structure electroceramics—NaDyTiO4, *J. Mater. Sci.*, 2005, **40**, 5419–5425.
49 A. Md Rahman and G. S. Chung, Synthesis of PVDF-graphene nanocomposites and their properties, *J. Alloys Compd.*, 2013, **581**, 724–730.
50 Y. Morita, T. Murata and K. Nakasuji, Cooperation of hydrogen-bond and charge-transfer interactions in molecular complexes in the solid state, *Bull. Chem. Soc. Jpn.*, 2013, **86**, 183–197.
51 G. Saito and Y. Yoshida, Development of conductive organic molecular assemblies: organic metals, superconductors, and exotic functional materials, *Bull. Chem. Soc. Jpn.*, 2007, **80**, 1–137.
52 O. Sato, Dynamic molecular crystals with switchable physical properties, *Nat. Chem.*, 2016, **8**, 644–656.
53 N. K. Nath, M. K. Panda, S. C. Sahoo and P. Naumov, Thermally induced and photoinduced mechanical effects in molecular single crystals—a revival, *CrystEngComm*, 2014, **16**, 1850–1858.
54 W. Zhang and R. G. Xiong, Ferroelectric metal–organic frameworks, *Chem. Rev.*, 2012, **112**, 1163–1195.
55 Y. Kamishina, Y. Akishige and M. Hashimoto, Ferroelectric Activity on Organic Crystal Trichloroacetamide, *J. Phys. Soc. Jpn.*, 1991, **60**, 2147–2150.
56 U. Venkataramudu, C. Sahoo, S. Leelashree, M. Venkatesh, D. Ganesh, S. R. G. Naraharisetty, A. K. Chaudhary, S. Srinath and R. Chandrasekar, Terahertz radiation and second-harmonic generation from a single-component polar organic ferroelectric crystal, *J. Mater. Chem. C*, 2018, **6**, 9330–9335.
57 P. Gruner-Bauer and E. Dormann, The ferroelectric low-temperature phase of single crystals of the substituted diacetylene 1,6-bis(2,4-dinitrophenoxy)-2,4-hexadiyne (DNP), *J. Phys.: Condens. Matter*, 1992, **4**, 5599.
58 S. Horiuchi, K. Kobayashi, R. Kumai and S. Ishibashi, Proton tautomerism for strong polarization switching, *Nat. Commun.*, 2017, **8**, 14426–14434.
59 A. J. Joseph, S. Goel, A. Hussain and B. Kumar, Ferro-/pyroelectric response of 0.57BF0.31PMN-0.12PT ternary ceramic far away from morphotropic phase boundaries, *Ceram. Int.*, 2017, **43**, 16676–16683.
60 D. Mao, B. Gnade and M. Q. Lopez, Ferroelectric properties and polarization switching kinetic of poly (vinylidene fluoride-trifluoroethylene) copolymer, *Ferroelectr.: Phys. Eff.*, 2011, 77–100.
61 J. E. Donaghey, A. Armin, D. M. Stoltzfus, P. L. Burn and P. Meredith, Correction: Dielectric constant enhancement of nonfullerene acceptors via side-chain modification, *Chem. Commun.*, 2016, **52**, 13714–13715.
62 A. Armin, D. M. Stoltzfus, J. E. Donaghey, A. J. Clulow, R. C. R. Nagiri, P. L. Burn, T. R. Gentle and P. Meredith, Engineering dielectric constants in organic semiconductors, *J. Mater. Chem. C*, 2017, **5**, 3736–3747.
63 A. R. WEST, *Solid state chemistry and its applications, 2nd ed.*, John Wiley & Sons Ltd, UK, 2014.
64 H. Pang, F. Zhang, M. Zeng, X. Gao, M. Qin, Lu Xubing, J. Gao, J. Dai and Q. Li, Preparation of epitaxial hexagonal $YMnO_3$ thin films and observation of ferroelectric vortex domains, *npj Quantum Mater.*, 2016, 16015.
65 H. Y. Zhang, N. Zhang, Y. Zhang, H. Y. Jiang, Y. L. Zeng, S. Y. Tang, P. F. Li, Y. Y. Tang and R. G. Xiong, Ferroelectric Phase Transition Driven by Switchable Covalent Bonds, *Phys. Rev. Lett.*, 2023, **28**(130), 176802.